

Geophysical Research Letters®

RESEARCH LETTER

10.1029/2021GL094476

Key Points:

- Mesoscale warm-core eddy sampled by rapid float profiling
- Spin-down by thermohaline intrusions dominates turbulent mixing
- Eddy transport across the northern Ross Gyre is limited by this thermohaline intrusion-eddy suppression mechanism

Correspondence to:

Y. Bebieva,
ybebieva3@gatech.edu

Citation:

Bebieva, Y., & Speer, K. (2021). Thermohaline suppression of upper circumpolar deep water eddies in the Ross Gyre. *Geophysical Research Letters*, 48, e2021GL094476. <https://doi.org/10.1029/2021GL094476>

Received 22 MAY 2021

Accepted 30 AUG 2021

Thermohaline Suppression of Upper Circumpolar Deep Water Eddies in the Ross Gyre

Yana Bebieva^{1,2}  and Kevin Speer¹

¹Geophysical Fluid Dynamics Institute, Florida State University, Tallahassee, FL, USA, ²School of Earth and Atmospheric Sciences, Georgia Institute of Technology, Atlanta, GA, USA

Abstract Temperature and salinity measurements of a warm-core eddy at the northern flank of the Ross Gyre are analyzed for dominant mixing mechanisms. The eddy is centered at the depths of the Circumpolar Deep Water and carries heat towards the gyre. Vertical and horizontal heat fluxes out of the eddy associated with internal wave turbulent mixing and thermohaline intrusions are estimated. Upward internal wave turbulent heat flux is $O(100)$ W/m², whereas, the lateral intrusive heat flux is of the order of $O(1000)$ W/m². The horizontal flux due to intrusions is suggested to be the dominant mechanism for eddy decay and yields an eddy lifetime of about 6 months. The thermohaline intrusion-eddy suppression mechanism is proposed and shown to be effective in suppressing the eddy field at the northern flank of the Ross Gyre. This effect has important implications for setting the basin-wide heat budget and regulating sea-ice cover.

Plain Language Summary The Southern Ocean Ross gyre separates the Antarctic Circumpolar Current (ACC) from the Antarctic continental margin. It carries warm water toward the continent at its eastern limit and brings cold freshwater from the continental margin into proximity with the ACC at its western boundaries. In this study, we examine a warm-core eddy that carries anomalous warm water towards the gyre center from the ACC. Estimates of vertical and horizontal heat fluxes indicate a short lifetime of such eddies (roughly 6 months). We propose that such eddies can be suppressed by thermohaline intrusions. Thus, the thermohaline intrusion-eddy suppression mechanism may regulate the overall heat budget within the Ross Gyre and influence sea-ice properties.

1. Introduction

The Weddell and Ross Gyres in the Southern Ocean separate the Antarctic Circumpolar Current (ACC) from the Antarctic continental margin. They carry warm water toward the continent at their eastern limit and bring cold fresh water from the continental margin into proximity with the ACC at their western limit. The gyres not only function as the dominant horizontal circulation cells but are a part of the three-dimensional meridional overturning circulation linking incoming deep waters from the north to the outgoing surface and bottom water flow (Marshall & Speer, 2012; Pellichero et al., 2018; Thompson et al., 2018), hence, a crucial intermediate step connecting the northern portions of the Southern Ocean with the Antarctic margins (e.g., Rintoul, 2018). The exchange processes within the gyres have a direct effect on upwelling deep water mass transformation (Abernathey et al., 2016; Bebieva & Speer, 2019), the formation of Antarctic Bottom Water (e.g., Jacobs et al., 1970) and the inflow of warm water delivered to ice shelves (Paolo et al., 2015; Rignot et al., 2013). Estimates of large-scale variability of the gyres (Armitage et al., 2018; Dotto et al., 2018; Fahrback et al., 1994) and exchange rates (Jullion et al., 2014; Roach & Speer, 2019) show an interplay between eddy fluxes, large-scale wind-driven gyre variability, and flow along the margin, with strong implications for lateral fluxes of freshwater.

In this study, we will focus on the exchange processes at the boundaries of the Ross Gyre. The strongest exchange with the ACC happens through the eastern boundary via seasonal variability of the gyre and eddy dynamics (Roach & Speer, 2019). Partial exchange at the northern boundary occurs mainly at fracture zones in the mid-ocean ridge. Elsewhere on the northern rim exchange appears to be weaker, possibly a result of a strong potential vorticity (PV) gradient acting as a barrier along the ACC, whereas this is absent on the eastern flank. This diagnostic is consistent with a limited exchange rate in the northern boundary of the Ross Gyre, but the governing physical processes setting this limit are not clear.

In this study, we propose a mechanism for the limited cross-gyre boundary exchange along the northern flank, despite the generation of eddies by instability along the ACC. We hypothesize that the eddy field at the gyre's northern boundary decays due to strong dissipation via thermohaline intrusions. In the North Atlantic Ocean lateral intrusions may significantly contribute to the decay of salty lenses known as "Meddies" originating in the Mediterranean outflow region (Hebert et al., 1990; Ruddick & Hebert, 1988). Here, we propose a similar mechanism. This mechanism is complementary to the suppression of lateral mixing by eddies due to mean flow effects on the eddy dispersion (Klocker et al., 2012; Naveira Garabato et al., 2011).

New high-frequency observations from 180° and 65°S (Figure 1a) revealed the presence of a warm-core eddy similar to a Meddy in the sense of a strong warm anomaly. The fine-scale observations of temperature and salinity show distinctly the thermohaline intrusions spreading through the eddy. This exposes a possible eddy decay mechanism that might be important for setting the large-scale properties of the gyre.

The paper is organized as follows. In the next section, we describe two sets of observations used in the study. In Section 3.1, we characterize the temperature and salinity fields of the observed eddy as well as derive the geostrophic velocity structure. We also infer a possible eddy generation site. Section 3.2 discusses different regimes of mixing at the eddy flanks. In Section 3.3, we compare and contrast the fluxes out of the eddy associated with internal wave turbulence and lateral thermohaline intrusions. Implications of the work are discussed in Section 4 and a summary is presented in Section 5.

2. Data

Two data sets were used in this study. The Argo data set of temperature and salinity profiles was used within the area bounded by 55°S and 75°S, 135°E and 90°W from January 1, 2010 to December 31, 2020. Argo data were mainly used to put the study in the broader context of the gyre circulation and variability. The vertical resolution of these profiles is 2 m in the shallow region and 10 m in the deeper regions, however, there are a few recent Argo floats with a vertical resolution of 0.25 m. The temporal resolution of the Argo float is 10 days. Some of the Argo floats are equipped with the ice avoidance mechanism (Wong & Riser, 2011), the GPS locations of the profiles taken under ice are interpolated between known GPS coordinates taken in open water. The nominal accuracy of the Argo salinity, temperature and depth measurements is ± 0.01 psu, ± 0.002 °C, and ± 2.4 m, respectively.

The second data set consists of high-resolution profiles delivered by an MRV float #11066 deployed from the N/R Laura Bassi on January 11, 2020 at 179°E and 66°S. This float was also programmed to avoid ice but this feature was not necessary over the short period of sampling reported here. The nominal accuracy of the MRV SBE CTD measurements is ± 0.004 mS/cm, ± 0.002 °C, and ± 0.25 m, respectively. The salinity data were adjusted following Sea-Bird Scientific dynamic correction algorithms to improve the precision at higher resolution. The float operated for 1 month and returned 49 profiles of temperature and salinity roughly every 12 h with vertical resolution of 1 m. Fortuitously, the float traversed through a warm-core eddy that is described in detail in the following section.

3. Characterization of the Warm-Core Eddy

3.1. Eddy Structure

Potential temperature and salinity cross sections show the convex lens structure indicating the anticyclonic flow (Figure 2). The eddy is centered at 300 m depth (based on the temperature anomaly) and spans the water column below the temperature minimum layer, known as Winter Water (WW), Mosby (1934). Along a transect through the eddy the maximum recorded temperature is 2.15 °C (Figure 2b) which is roughly 0.75 °C warmer than the surrounding water (Figure 1c). The eddy core is also fresher than its environment by about 0.1 on pressure levels (Figure 1d), but saltier than the environment by 0.06 following isopycnals (Figure 2d). Given the eddy core properties, it likely originated to the northwest at the ACC (Figures 1a and 1b). Assuming a straight path from an inferred origin site of the eddy to its observed location (~900 km, Figure 1a) and a characteristic speed of ACC of $O(1)$ ms^{-1} (Whitworth, 1983), a low bound on the eddy age is about 1 week. It is also worth pointing that if such eddies persisted in wintertime, the warm core of an eddy would underlie a cold surface mixed layer, and vertical fluxes would directly impact sea-ice growth rates.

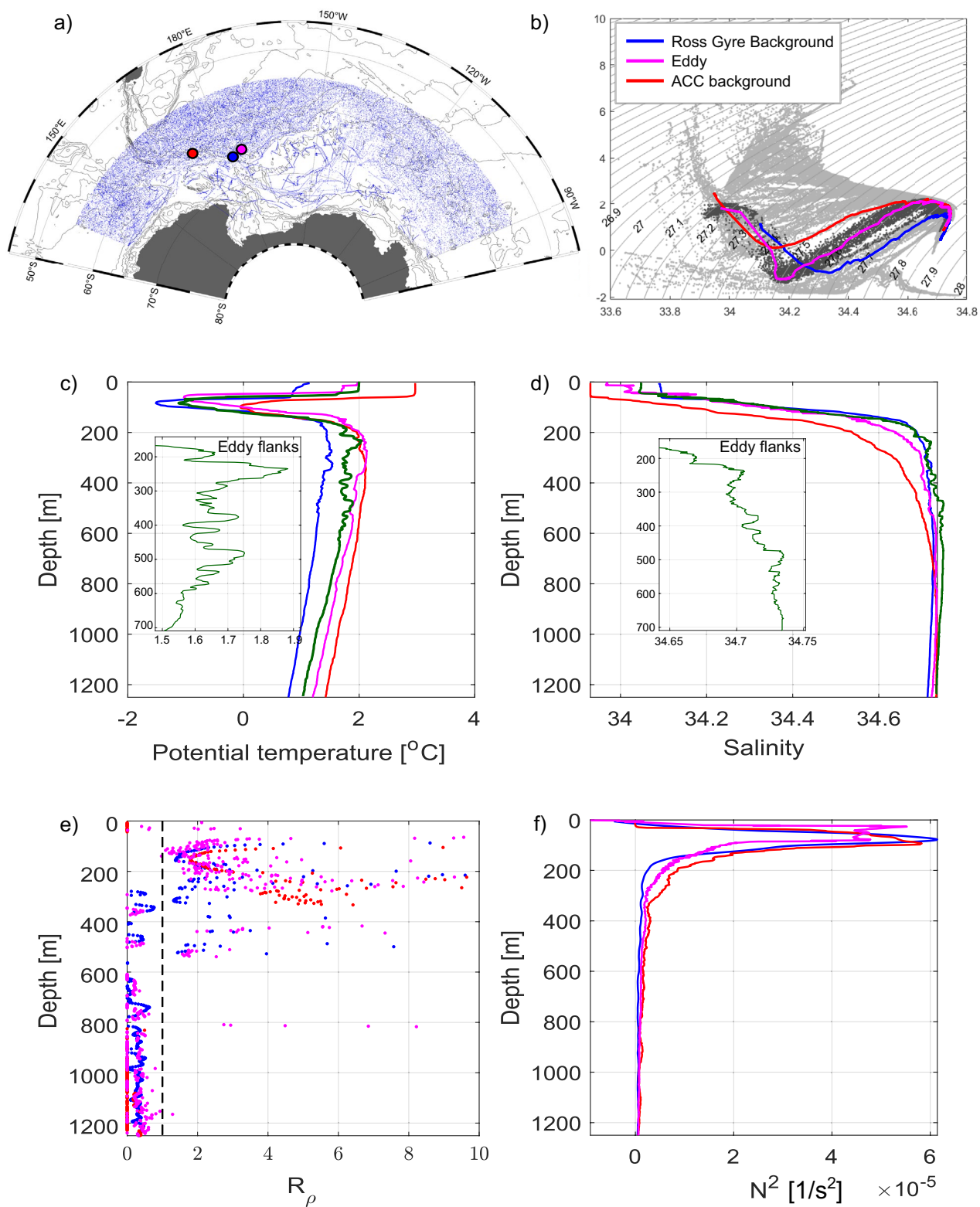


Figure 1.

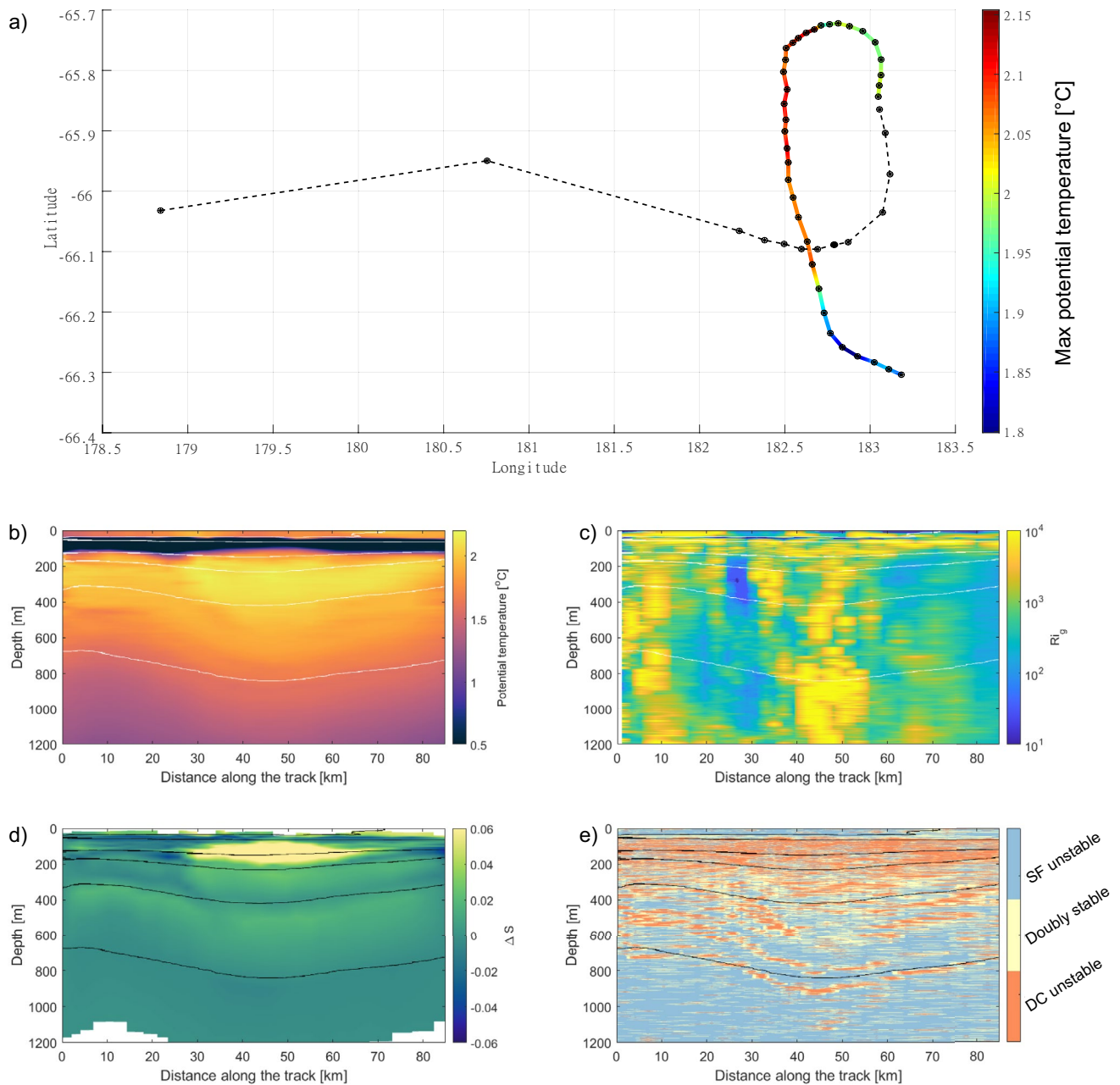


Figure 2. (a) The float drift track with colors representing maximum potential temperature recorded from January 31, 2020 to February 16, 2020. Dashed line shows positions of the profiles with maximum depth shallower than 600 m. Sections along the colored portion of the drift track shown in (a) represent (b) potential temperature, (c) Richardson number, (d) isopycnal salinity anomaly defined as difference between the eddy and background Ross Gyre, and (e) Turner angle marked by diffusive convective unstable ($-90 < Tu < -45$), doubly stable ($-45 < Tu < 45$), and salt fingering unstable ($45 < Tu < 90$) regimes. White contours in (b–c) and black contours in (d–e) are isopycnals (potential density relative to zero pressure, kg m^{-3}).

Figure 1. (a) Map showing a region of the Ross Gyre where Argo floats (blue dots) were operating from January 1, 2010 to December 31, 2020. Purple dot shows the location of the eddy sampled by an MRV float #11066. The blue and red dots show the Argo profile locations shown in (b–f). (b) Temperature and salinity diagram showing all the profiles within the Ross Gyre area (light gray dots); dark gray dots show the measurements that belong to the eddy; the purple line shows typical $\theta - S$ properties within the eddy core; the red line shows typical $\theta - S$ within the Antarctic Circumpolar Current, and the blue line shows a typical profile for the Ross Gyre. (c) Potential temperature and (d) salinity profiles of the locations discussed above; the green lines show the profile taken through the eddy flank. (e) Vertical density ratio R_ρ and (f) The Brunt-Väisälä frequency N^2 .

3.1.1. Eddy Temperature and Salinity Properties

When both temperature θ and salinity S increase or decrease with depth, stratification is amenable to double-diffusive instability. In the northwestern portion of the Ross Gyre there are depth ranges where this occurs. In the depth range between about 100 and 200 m, both θ and S increase, hence, this layer is prone to the diffusive convection (DC) type of double diffusion. Below 600 m, both θ and S decrease, and therefore this layer is prone to salt-fingering (SF). Between 200 and 600 m the vertical gradients in θ and S are minimal as this is the depth of the Upper Circumpolar Deep Water (UCDW) where maxima in θ and S are observed. The susceptibility of the background stratification to double-diffusive processes (either DC or SF) is usually characterized with the background vertical density ratio $\overline{R}_\rho = \beta \overline{S}_z / \alpha \overline{\theta}_z$, where $\overline{\theta}_z$ and \overline{S}_z are vertical bulk gradients of potential temperature and salinity. We used linearly approximated profiles within 15 m window to smooth out high frequency fluctuations; $\alpha = -(1/\rho_0)(\partial\rho/\partial\theta)_{s,p}$ is the thermal expansion coefficient, and $\beta = (1/\rho_0)(\partial\rho/\partial S)_{\theta,p}$ is the saline contraction coefficient (ρ is density, ρ_0 is a reference density, and p is pressure). When $\overline{R}_\rho > 1$ the stratification is DC-amenable (Figure 1e, 100–200 m) and when $\overline{R}_\rho < 1$ SF-amenable (Figure 1e, below 600 m).

The transect through the eddy dramatically indicates multiple thermohaline intrusions at depths between 200 and 600 m. These intrusions are self-driven laterally propagating water masses which are manifested by vertically alternating DC and SF regions (insets in Figures 1c and 1d). The intrusions are coherent throughout the eddy and can be visualized using the Turner angle, \overline{Tu} (Ruddick, 1983). Tu is a function of \overline{R}_ρ that is often used due to less ambiguity than \overline{R}_ρ with its infinite ranges and vagueness of sign (when $R_\rho < 0$, a water column might be either doubly stable or statically unstable). The Turner angle is defined as

$$\overline{Tu} = \tan^{-1} \left(\frac{1 + \overline{R}_\rho}{1 - \overline{R}_\rho} \right) \quad (1)$$

When $-90^\circ < \overline{Tu} < -45^\circ$, the water column is DC unstable; and when $45^\circ < \overline{Tu} < 90^\circ$, the water column is SF unstable. The water column is doubly stable when $-45^\circ < \overline{Tu} < 45^\circ$. Figure 2e clearly shows alternating DC and SF bands that span the eddy laterally.

The intrusions are more prominent (i.e., more frequent interleaving with smaller vertical wavelength) at the eddy flanks, which is typical for “meddy”-like eddies (Bebieva & Timmermans, 2016; Fine et al., 2018; Hebert et al., 1990; Ruddick & Hebert, 1988) (Figures 1c, 1d and 2e).

3.1.2. Eddy Velocity Structure

To characterize eddy velocity structure, we assume that the eddy is in cyclogeostrophic balance

$$\frac{v_c^2}{r} + f v_c - \frac{1}{\rho_0} \frac{\partial p}{\partial r} = 0, \quad (2)$$

where v_c is the cyclogeostrophic velocity, r is distance from the eddy center, p is the pressure, ρ_0 is a reference density, and $f = -1.33 \times 10^{-4}$ is the Coriolis parameter. The velocity can be computed by first estimating the geostrophic velocity, v_g , between two adjacent profiles using dynamic heights and assuming a level-of-no-motion of 1,250 m depth (which is the deepest common depth of the data set) in the integration. Then the cyclogeostrophic velocity can be expressed as $v_c = 0.5 \left[-fr - \sqrt{f^2 r^2 + 4frv_g} \right]$. Here, we assume that the float crossed the eddy through its center. The computations show that the cyclogeostrophic velocity is only ~4% bigger compared to the geostrophic velocity, therefore, we will use the geostrophic velocity in the following.

To determine the eddy dimension, we assume that it is axisymmetric and in solid-body rotation. By fitting an idealized Rankine vortex model (which is consistent with previous observations of eddies in the Southern Ocean, e.g., Martinson & McKee, 2012) to the computed velocity

$$V(r) = \begin{cases} \frac{V_{max} r}{R}, & \text{if } r < R \\ \frac{V_{max} R}{r}, & \text{if } r > R \end{cases} \quad (3)$$

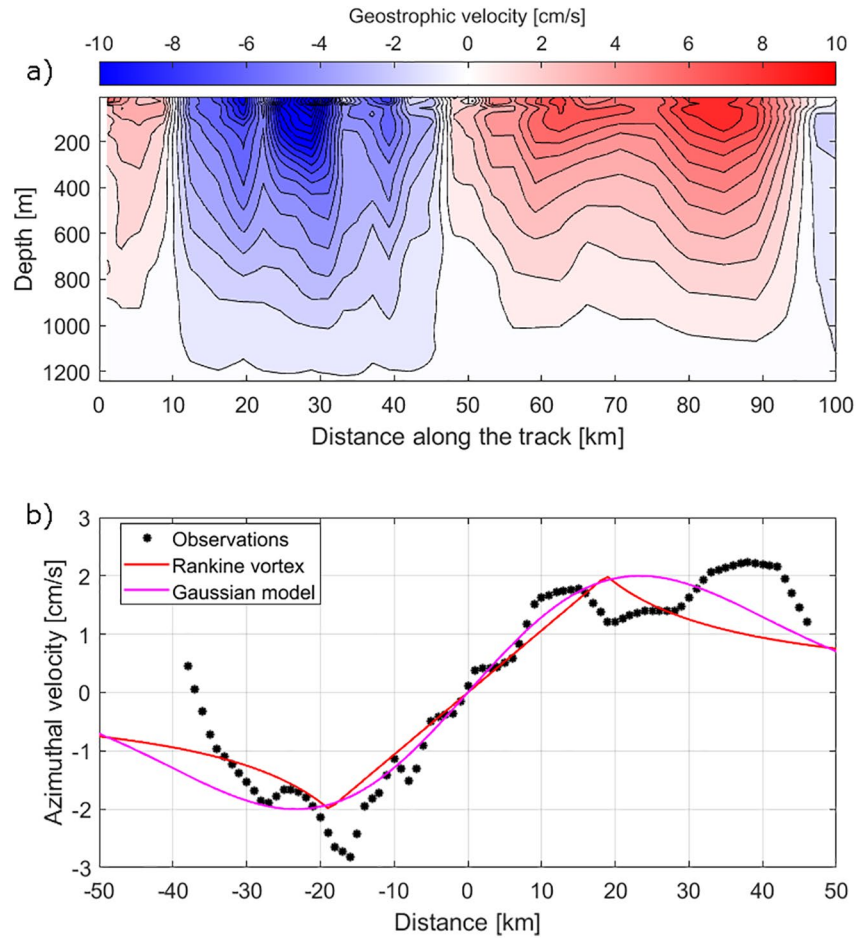


Figure 3. (a) A north-south section of cyclogeostrophic velocity through the eddy with a level of no-motion of 1,250 m corresponding to the deepest levels sampled by the float. Only the central portion of the section represents the velocity within the eddy. (b) Eddy cyclogeostrophic velocity at 75 m corresponding to the depth of maximum v_g from (a). Zero distance corresponds to the core position of the eddy. The red line represents the Rankine vortex model (2) and the magenta line represents the Gaussian model (3).

we can estimate the maximum azimuthal velocity of the eddy V_{max} and its radius R . Another approximation of the velocity structure is a Gaussian model (von Appen et al., 2014):

$$V(r) = V_{max} \frac{r}{R} \exp \left[\frac{1}{2} \left(1 - \left(\frac{r}{R} \right)^2 \right) \right]. \quad (4)$$

Both models (3) and (4) give a similar characterization of the eddy with $V_{max} \approx 0.02 \text{ m s}^{-1}$ and $R = 20 \text{ km}$ (Figure 3). For an eddy in solid-body rotation, these parameters yield a Rossby number $Ro = 2V_{max}/fR \approx 0.02$ (for scaling see, e.g., Manley & Hunkins, 1985). The eddy radius is similar but somewhat larger than the internal Rossby radius of deformation for the ACC front near 62°S , $R_d = \sqrt{g'h/f} \approx 7 \text{ km}$ (Chelton et al., 1998), if we consider the stratification in a two-layer framework with the shallow layer being the mixed layer of thickness $\sim 100 \text{ m}$ and density $1,027 \text{ kg m}^{-3}$, and the lower layer of density $1,027.75 \text{ kg m}^{-3}$.

3.2. Regimes of Mixing: Theoretical Formulation

There are at least three potential mechanisms by which heat and salt anomalies within the eddy core can be mixed with the ambient water: vertical shear-driven mixing due to internal wave breaking, vertical

double-diffusive mixing in the regions susceptible to the double-diffusive instability, and lateral heat transfer by thermohaline intrusions.

Visual inspection of the profiles throughout the eddy suggests that the vertical turbulent mixing overwhelms double-diffusive mixing. That is, in the regions that are salt fingering and diffusive convective unstable, $-90 < Tu < -45$ and $45 < Tu < 90$ respectively (Figure 2e), double-diffusive staircases are smeared out by the turbulent mixing and are not observed (as described in Bebieva and Timmermans [2016]). Thus, we conclude that double-diffusive mixing at the top and bottom of the eddy does not play a role in vertical heat and salt transfer. Intrusions can be initiated through baroclinic instability on the edges of eddies (May & Kelley, 2001). However, double-diffusive mixing may play a dominant role in setting up thermohaline intrusions and thus impact lateral heat transfer (Bebieva & Timmermans, 2017, 2019). Below we consider in detail two remaining types of mixing: internal wave breaking and thermohaline intrusions.

3.2.1. Internal Wave Turbulence

Assuming that the turbulent mixing associated with breaking internal waves is the dominant mixing at the top and bottom of the eddy we use a strain-based fine-scale parameterization to estimate the dissipation rate of the turbulent kinetic energy, ϵ , in these regions. We follow the approach discussed in Kunze et al. (2006)

$$\epsilon_{IW} = \epsilon_0 \frac{\overline{N^2}}{N_0^2} \frac{\langle \xi_z^2 \rangle^2}{\langle \xi_{zGM}^2 \rangle^2} h(R_\omega) L(f, \bar{N}) \quad (5)$$

where $\epsilon_0 = 6.73 \times 10^{-10} \text{W/kg}$ and $N_0 = 5.24 \times 10^{-3} \text{s}^{-1}$ based on normalization by the Garrett-Munk spectrum (Garrett & Munk, 1979). The average background stratification is denoted with $\overline{N^2}$, computed as $N^2 = -(g/\rho)(\partial\rho/\partial z)$, where z is depth and $g = 9.8 \text{ms}^{-2}$ is gravitational acceleration. Angle brackets represent integrated variables over the internal wavefield vertical wavenumbers. The functions $h(R_\omega)$ and $L(f, \bar{N})$ represent the effects of the internal wavefield frequency content and corrections for a latitudinal dependence. Given the absence of small-scale shear data, we take the global average $R_\omega = 7$ (Chanona et al., 2018; Kunze et al., 2006). This fine-scale parameterization is applicable only at the depths where the stratification is relatively weak and shows minimal variation (Polzin et al., 2014). In the depth range at the top (100–200 m) and bottom (500–700 m) of the eddy, N varies by less than a factor of two (Figure 1f).

Following the methodology of Chanona et al. (2018) the wave-induced strain $\xi_z = (N^2 - N_{ref}^2)/N_{ref}^2$, where N is computed on 1-dbar grid and the background stratification N_{ref} is evaluated using a smooth piecewise quadratic fit to the observed profiles with a window of 10 m. We found that the resulting ϵ is not significantly sensitive to the fitting window and it changes by a few percent upon increasing or decreasing the window by 3 m. All levels are below the surface mixed layer, which is identified as the depth at which density increases by 0.02kg/m^3 (Arrigo et al., 1999; Bebieva & Speer, 2019; Pellichero et al., 2017; Sweeney et al., 2000; Shaw & Stanton, 2014).

Next, applying a fast Fourier transform on ξ_z as a function of vertical wavenumber we obtain $\langle \xi_z^2 \rangle$ by integrating the spectra between the vertical wavenumbers $k_{zmin} = 0.02 \text{cpm}$ and $k_{zmax} = 0.1 \text{cpm}$ (corresponding to $\lambda_{zmin} = 50 \text{m}$ and $\lambda_{zmax} = 10 \text{m}$, respectively) (Chanona et al., 2018).

To compute the diapycnal eddy diffusivity associated with the internal wave-driven mixing K_{IW} , we apply the standard Osborn (1980) formulation

$$K_{IW} = \Gamma \frac{\epsilon_{IW}}{N^2}, \quad (6)$$

where Γ is the flux coefficient that is commonly assumed to be 0.2 for the internal wave mixing when turbulence is fully developed (Smyth et al., 2001), although we note that this might be a source of uncertainty. There is also strain associated with unbalanced flow within the eddy and curvature of the isopycnals; however, this is expected to be less important due to the small Rossby number (e.g., Shakespeare, 2016). Using the standard Fick's law of diffusion, the vertical heat flux out of the eddy is estimated as

$$F_{IW}^0 = -\rho c_p K_{IW} \overline{\theta_z}, \quad (7)$$

where, overbar denotes background gradient estimated within a 10 m depth window, ρ is a reference density and c_p is the specific heat of seawater.

3.2.2. Lateral Thermohaline Intrusions

To estimate lateral heat associated with the thermohaline intrusions we employ the Joyce et al. (1978) model. It describes the production-dissipation balance between the production of thermal anomalies due to lateral advection along intrusions and destruction of these anomalies by diapycnal mixing

$$\tilde{u}\tilde{\theta}\frac{\partial\bar{\theta}}{\partial x} = K_{\theta}\left(\frac{\partial\bar{\theta}}{\partial z}\right)^2, \quad (8)$$

where $\tilde{u}\tilde{\theta}$ represents the lateral intrusion heat flux ($F_{int}^{\theta} = \rho c_p \tilde{u}\tilde{\theta}$), $\partial\bar{\theta}/\partial x$ is the horizontal cross-frontal gradient averaged over intrusion scale, K_{θ} vertical diapycnal diffusivity within intrusions and $\partial\bar{\theta}/\partial z$ is vertical gradient averaged on the intrusion scale. The vertical and horizontal gradients can be estimated from the fine-scale observations, however, K_{θ} can be derived either from microstructure data (based on dissipation of the turbulent kinetic energy) or estimated using various parameterization schemes. For this reason, K_{θ} may produce a large source of uncertainty. The nominal value of K_{θ} that is usually used in intrusion studies is $10^{-4} \text{ m}^2 \text{ s}^{-1}$, assumed to be constant (Ruddick & Kerr, 2003).

3.3. Estimates of Effective Diffusivities and Fluxes

Using the MRV data we estimate the effective diffusivities and heat fluxes at upper and lower layers of the eddy (associated with the turbulent mixing) and central portion (associated with the intrusions).

Following Equation 7 and with a vertical temperature gradient at the top and bottom of the eddy of $O(10^{-2})^{\circ} \text{ C m}$ and $O(10^{-3})^{\circ} \text{ C m}$ from the observations (Figure 2b), we obtain $O(100) \text{ W/m}^2$ upward and $O(1) \text{ W/m}^2$ downward heat fluxes out of the eddy due to turbulent mixing associated with the internal waves. Here, we used $K_{IW} \approx 10^{-3} \text{ m}^2 \text{ s}^{-1}$ at the top of the eddy and $K_{IW} \approx 5.6 \times 10^{-4} \text{ m}^2 \text{ s}^{-1}$ at the bottom of the eddy (Figure 5).

To estimate the lateral heat flux out of the eddy we follow Equation 8. Based on the eddy characteristics with the temperature anomaly of 0.75° and the radius of $R = 20 \text{ km}$, $\partial\bar{\theta}/\partial x = O(10^{-5})^{\circ} \text{ C m}$ (Figure 2b). The intrusion structures at the eddy flanks (Figure 1c) imply $\partial\bar{\theta}/\partial z = O(10^{-2})^{\circ} \text{ C m}$. Assuming $K_{\theta} = 10^{-4} \text{ m}^2 \text{ s}^{-1}$, the lateral intrusion heat flux is $F_{int}^{\theta} = O(1000) \text{ W/m}^2$.

Given the two flux estimates, it is of interest to assess the eddy lifetime. Simple scaling analysis based on diffusion timescales yields an eddy dissipation time due to vertical internal wave mixing $\tau_{IW} = H^2/K_{IW} = 6 \times 10^8 \text{ s} \approx 11 \text{ years}$. Whereas the lateral mixing due to intrusions would eliminate the temperature anomaly over $\tau_{IW} = R^2/K_{int} = 1.6 \times 10^7 \text{ s} \approx 0.5 \text{ years}$, where $K_{int} = 25 \text{ m}^2 \text{ s}^{-1}$ is the lateral diffusivity estimated based on the lateral heat flux and lateral temperature gradient. This horizontal diffusivity falls within a typical range of lateral diffusivities $5\text{--}50 \text{ m}^2 \text{ s}^{-1}$ for the double-diffusive system (Hebert et al., 1990; Walsh & Carmack, 2003). These estimates indicate that intrusions are more efficient in eddy dissipation compared to vertical turbulent mixing. In fact, recent direct numerical simulations of salt lenses showed that the lateral flux due to intrusions is dominant in the eddy decay process and the vertical mixing has an adverse effect on the eddy dispersion (extends the eddy lifetime) by suppressing the interleaving (Radko & Sisti, 2017).

4. Implications for the Large-Scale Circulation of the Ross Gyre

The short lifetime of the warm-core eddy of several months suggests an “arresting” mechanism of the eddy field by thermohaline intrusions. This implies that the southward transport of the UCDW heat into the gyre from the ACC fronts is strongly suppressed due to intrusive fluxes. To put this effect in the context of a larger Ross Gyre circulation, we examine profiles at the gyre boundary for intrusions.

To assess the horizontal variability of intrusive features in the gyre, the Argo data set was averaged onto a 4° longitude by 0.5° latitude grid (Figures 4a and 4b). We introduce an intrusion index $\mathcal{I} = N_i/N_p$, where N_i is the total number of inversions (defined as regions in depth where, both θ and S decrease) per grid cell and N_p is the total number of the profiles within that grid cell. According to this definition $\mathcal{I} = 1$ implies that there is at least one intrusion per profile within a given grid point. A larger \mathcal{I} means there are multiple intrusions per profile. Figure 4c shows that the region near 180° and 65°S is the area where the maximum number of intrusions is observed. \mathcal{I} is also large along the northern rim of the gyre, but takes much smaller

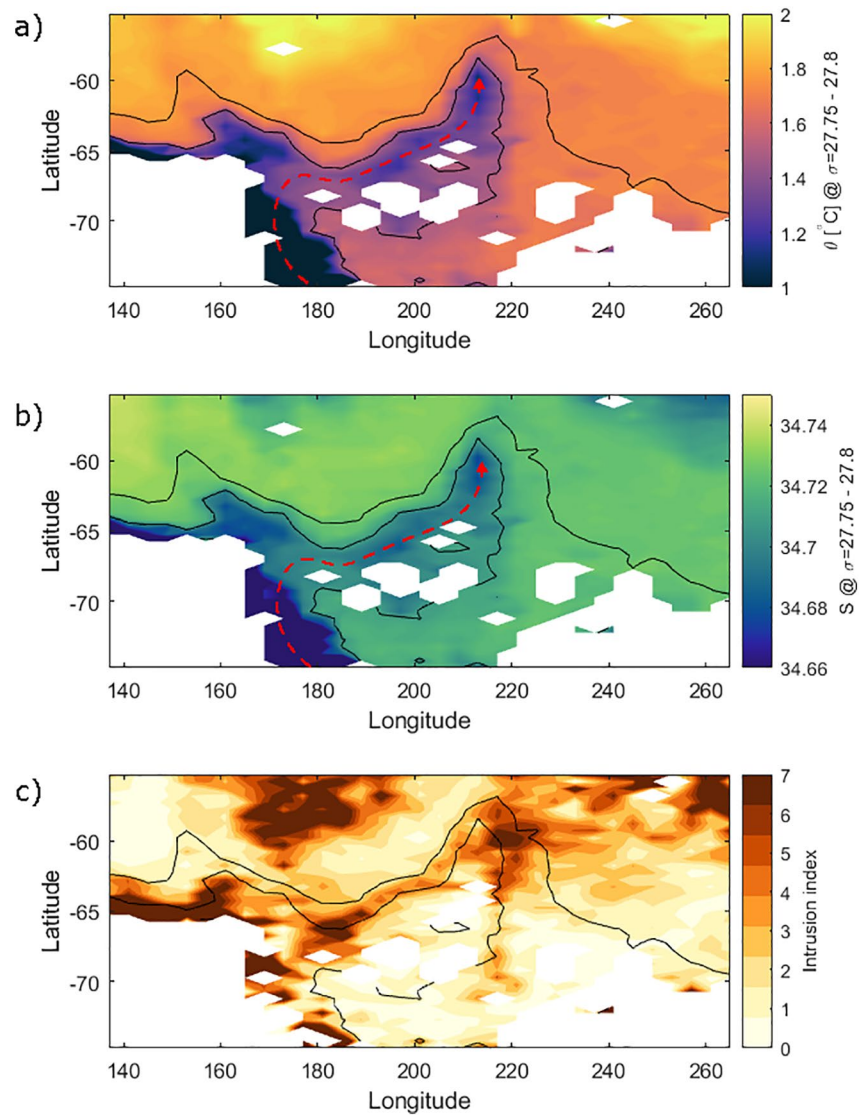


Figure 4. Maps of (a) Potential temperature and (b) salinity both averaged between the density band of $\sigma = 27.75$ kg/m^3 and $\sigma = 27.8$ kg/m^3 . Red dashed arrows show schematically the pathway of the glacial meltwater. (c) Map of intrusion index (see the definition in text).

values at the eastern portion of the gyre. The thickness of intrusion inversions suggests that the intrusions around the northern portion of the Ross Gyre have a similar structure as those observed within the warm-core eddy discussed above. The profiles in the analysis are derived from the Argo data set; given the spatial and temporal resolution of the Argo data set, it is not possible to determine whether or not these profiles belong to eddies. However, it is not unreasonable to assume so as the properties of the profiles with large ∇ (not shown here) resemble the eddy profiles.

This analysis indicates that the eddy field in the northern portion of the Ross Gyre is suppressed by the intrusions. On the eastern portion of the gyre, in contrast, the intrusions are rarely present (Figure 4c). We hypothesize that the abundance of intrusions in the northern boundary is due to the stronger lateral gradient in temperature and salinity (Figures 4a and 4b) centered around the UCDW depths ($\sigma = 27.75 - 27.8$ kg/m^3). We speculate that this is because the fresher and cooler glacial melt water at these densities circulates clock-wise around the gyre and forms a strong front when it encounters the warm and salty ACC (shown schematically by the dashed arrows in Figures 4a and 4b).

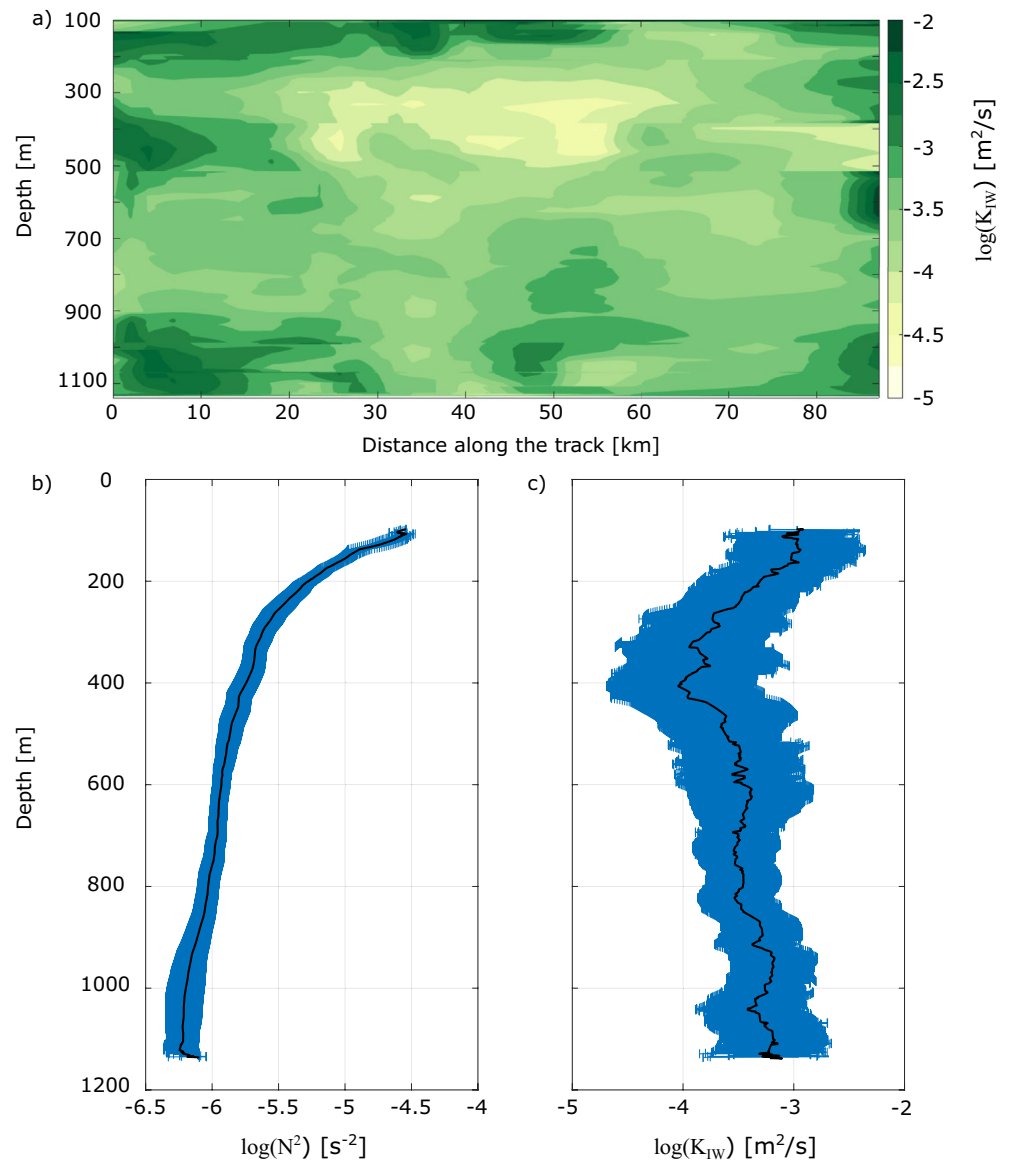


Figure 5. (a) Depth-distance section along the colored portion of the drift track shown in Figure 2a showing the base 10 logarithm of effective eddy diffusivity $\log_{10}(K_{IW})$. (b) The base 10 logarithm of the mean vertical profile of the Brunt-Vaisala frequency N^2 (black line). (c) The mean vertical profile of $\log_{10}(K_{IW})$ (black line). Blue shading in (b) and (c) shows one standard deviation.

5. Summary

Two major mixing processes are inferred for ACC warm-core eddies that cause the eddy temperature anomaly to dissipate. Vertical turbulent heat flux associated with breaking internal waves accounts for $O(100)$ W/m^2 out of the eddy. Lateral fluxes out of the eddy are one magnitude larger $O(1,000)$ W/m^2 , yielding an eddy decay timescale of several months. A short lifetime of warm core eddies implies that the inflow of the warm UCDW into the gyre is limited in this zone by strong thermohaline gradients.

We hypothesize that inflow of subsurface fresher and cooler waters around the gyre makes the lateral temperature and salinity gradients stronger at the northern flank (Figures 4a and 4b). As the eddies with anomalously warm core enter the gyre from the north, the strong difference in properties promotes the formation of intrusions on eddy flanks which eventually dissipate an eddy. This mechanism shuts off the eddy transport in the northern part of the Ross Gyre consistent with Roach and Speer (2019).

The accumulation of fresh and cold water within the gyre not only limits the inflow of the UCDW into the gyre through thermohaline intrusion-eddy suppression mechanism, but also can regulate the sea-ice cover. The warm core of UCDW eddies located below the WW implies that in winter season upward heat fluxes from the eddy core would go directly into the mixed layer and thus impact sea ice. More observations with fine spatial and temporal resolution are needed to gain a more complete view of the significance of the proposed suppression mechanism.

Data Availability Statement

Argo data were collected and made freely available by the International Argo Program and the national programs that contribute to it. (<https://argo.ucsd.edu>, <https://www.ocean-ops.org>). The Argo Program is part of the Global Ocean Observing System. The Argo temperature and salinity profiles was used within the area bounded by 55°S and 75°S, 135°E and 90°W from January 1, 2010 to December 31, 2020. The MRV data used in this study are openly available at <https://www.ncei.noaa.gov/archive/accession/0240501>, float number 11066.

Acknowledgments

The authors thank Pierpaolo Falco and CSIRO for help deploying the floats, and Kim Martini for providing support in implementing thermal corrections to the data. Special thanks to Melanie Chanona and Stephanie Waterman for providing the algorithm for computing wave-induced strain from CTD profiles. The authors thank two anonymous reviewers for their constructive and thoughtful reviews. Funding was provided by NSF OPP-1643679 and OCE-1658479.

References

- Abernathy, R. P., Cerveck, I., Holland, P. R., Newsom, E., Mazloff, M., & Talley, L. D. (2016). Water-mass transformation by sea ice in the upper branch of the Southern Ocean overturning. *Nature Geoscience*, 9(8), 596–601. <https://doi.org/10.1038/ngeo2749>
- Armitage, T. W., Kwok, R., Thompson, A. F., & Cunningham, G. (2018). Dynamic topography and sea level anomalies of the Southern Ocean: Variability and teleconnections. *Journal of Geophysical Research: Oceans*, 123(1), 613–630. <https://doi.org/10.1002/2017jc013534>
- Arrigo, K. R., Robinson, D. H., Worthen, D. L., Dunbar, R. B., DiTullio, G. R., VanWoert, M., & Lizotte, M. P. (1999). Phytoplankton community structure and the drawdown of nutrients and in the Southern Ocean. *Science*, 283(5400), 365–367. <https://doi.org/10.1126/science.283.5400.365>
- Bebieva, Y., & Speer, K. (2019). The regulation of sea ice thickness by double-diffusive processes in the Ross Gyre. *Journal of Geophysical Research: Oceans*, 124(10), 7068–7081. <https://doi.org/10.1029/2019jc015247>
- Bebieva, Y., & Timmermans, M.-L. (2016). An examination of double-diffusive processes in a mesoscale eddy in the Arctic Ocean. *Journal of Geophysical Research: Oceans*, 121(1), 457–475. <https://doi.org/10.1002/2015jc011105>
- Bebieva, Y., & Timmermans, M.-L. (2017). The relationship between double-diffusive intrusions and staircases in the Arctic Ocean. *Journal of Physical Oceanography*, 47(4), 867–878. <https://doi.org/10.1175/jpo-d-16-0265.1>
- Bebieva, Y., & Timmermans, M.-L. (2019). Double-diffusive layering in the Canada Basin: An explanation of along-layer temperature and salinity gradients. *Journal of Geophysical Research: Oceans*, 124(1), 723–735. <https://doi.org/10.1029/2018jc014368>
- Chanona, M., Waterman, S., & Gratton, Y. (2018). Variability of internal wave-driven mixing and stratification in Canadian Arctic shelf and shelf-slope waters. *Journal of Geophysical Research: Oceans*, 123(12), 9178–9195. <https://doi.org/10.1029/2018jc014342>
- Chelton, D. B., DeSzoeke, R. A., Schlax, M. G., El Naggar, K., & Siwertz, N. (1998). Geographical variability of the first baroclinic Rossby radius of deformation. *Journal of Physical Oceanography*, 28(3), 433–460. [https://doi.org/10.1175/1520-0485\(1998\)028<0433:gvotfb>2.0.co;2](https://doi.org/10.1175/1520-0485(1998)028<0433:gvotfb>2.0.co;2)
- Dotto, T. S., Naveira Garabato, A., Bacon, S., Tsamados, M., Holland, P. R., Hooley, J., et al. (2018). Variability of the Ross Gyre, southern ocean: Drivers and responses revealed by satellite altimetry. *Geophysical Research Letters*, 45(12), 6195–6204. <https://doi.org/10.1029/2018gl078607>
- Fahrbach, E., Rohardt, G., Schröder, M., & Strass, V. (1994). Transport and structure of the Weddell Gyre. *Annales Geophysicae*, 12, 840–855. <https://doi.org/10.1007/s00585-994-0840-7>
- Fine, E. C., MacKinnon, J. A., Alford, M. H., & Mickett, J. B. (2018). Microstructure observations of turbulent heat fluxes in a warm-core Canada Basin eddy. *Journal of Physical Oceanography*, 48(10), 2397–2418. <https://doi.org/10.1175/jpo-d-18-0028.1>
- Garrett, C., & Munk, W. (1979). Internal waves in the ocean. *Annual Review of Fluid Mechanics*, 11(1), 339–369. <https://doi.org/10.1146/annurev.fl.11.010179.002011>
- Hebert, D., Oakey, N., & Ruddick, B. (1990). Evolution of a Mediterranean salt lens: Scalar properties. *Journal of Physical Oceanography*, 20(9), 1468–1483. [https://doi.org/10.1175/1520-0485\(1990\)020<1468:eoamsl>2.0.co;2](https://doi.org/10.1175/1520-0485(1990)020<1468:eoamsl>2.0.co;2)
- Jacobs, S. S., Amos, A. F., & Bruchhausen, P. M. (1970). Ross sea oceanography and Antarctic bottom water formation. *Deep Sea Research and Oceanographic Abstracts*, 17, 935–962. [https://doi.org/10.1016/0011-7471\(70\)90046-x](https://doi.org/10.1016/0011-7471(70)90046-x)
- Joyce, T. M., Zenk, W., & Toole, J. M. (1978). The anatomy of the Antarctic polar front in the Drake Passage. *Journal of Geophysical Research: Oceans*, 83(C12), 6093–6113. <https://doi.org/10.1029/jc083ic12p06093>
- Jullion, L., Garabato, A. C. N., Bacon, S., Meredith, M. P., Brown, P. J., Torres-Valdés, S., et al. (2014). The contribution of the Weddell Gyre to the lower limb of the Global Overturning Circulation. *Journal of Geophysical Research: Oceans*, 119(6), 3357–3377. <https://doi.org/10.1002/2013jc009725>
- Klocker, A., Ferrari, R., & LaCasce, J. H. (2012). Estimating suppression of eddy mixing by mean flows. *Journal of Physical Oceanography*, 42(9), 1566–1576. <https://doi.org/10.1175/jpo-d-11-0205.1>
- Kunze, E., Firing, E., Hummon, J. M., Chereskin, T. K., & Thurnherr, A. M. (2006). Global abyssal mixing inferred from lowered ADCP shear and CTD strain profiles. *Journal of Physical Oceanography*, 36(8), 1553–1576. <https://doi.org/10.1175/jpo2926.1>
- Manley, T., & Hunkins, K. (1985). Mesoscale eddies of the Arctic Ocean. *Journal of Geophysical Research*, 90(C3), 4911–4930. <https://doi.org/10.1029/jc090ic03p04911>
- Marshall, J., & Speer, K. (2012). Closure of the meridional overturning circulation through Southern Ocean upwelling. *Nature Geoscience*, 5(3), 171–180. <https://doi.org/10.1038/ngeo1391>

- Martinson, D., & McKee, D. (2012). Transport of warm Upper Circumpolar Deep Water onto the western Antarctic Peninsula continental shelf. *Ocean Science*, 8(4). <https://doi.org/10.5194/os-8-433-2012>
- May, B. D., & Kelley, D. E. (2001). Growth and steady state stages of thermohaline intrusions in the Arctic Ocean. *Journal of Geophysical Research: Oceans*, 106(C8), 16783–16794. <https://doi.org/10.1029/2000jc000605>
- Mosby, H. (1934). *The waters of the Atlantic Antarctic Ocean*. Jacob Dybwad.
- Naveira Garabato, A. C., Ferrari, R., & Polzin, K. L. (2011). Eddy stirring in the Southern Ocean. *Journal of Geophysical Research*, 116(C9), C09019. <https://doi.org/10.1029/2010jc006818>
- Osborn, T. (1980). Estimates of the local rate of vertical diffusion from dissipation measurements. *Journal of Physical Oceanography*, 10(1), 83–89. [https://doi.org/10.1175/1520-0485\(1980\)010<0083:eotro>2.0.co;2](https://doi.org/10.1175/1520-0485(1980)010<0083:eotro>2.0.co;2)
- Paolo, F. S., Fricker, H. A., & Padman, L. (2015). Volume loss from Antarctic ice shelves is accelerating. *Science*, 348(6232), 327–331. <https://doi.org/10.1126/science.aaa0940>
- Pellichero, V., Sallée, J.-B., Chapman, C. C., & Downes, S. M. (2018). The Southern Ocean meridional overturning in the sea-ice sector is driven by freshwater fluxes. *Nature Communications*, 9(1), 1–9. <https://doi.org/10.1038/s41467-018-04101-2>
- Pellichero, V., Sallée, J.-B., Schmidtke, S., Roquet, F., & Charrassin, J.-B. (2017). The ocean mixed layer under Southern Ocean sea-ice: Seasonal cycle and forcing. *Journal of Geophysical Research: Oceans*, 122(2), 1608–1633. <https://doi.org/10.1002/2016jc011970>
- Polzin, K. L., Garabato, A. C. N., Huussen, T. N., Sloyan, B. M., & Waterman, S. (2014). Finescale parameterizations of turbulent dissipation. *Journal of Geophysical Research: Oceans*, 119(2), 1383–1419. <https://doi.org/10.1002/2013jc008979>
- Radko, T., & Sisti, C. (2017). Life and demise of intrathermocline mesoscale vortices. *Journal of Physical Oceanography*, 47(12), 3087–3103. <https://doi.org/10.1175/jpo-d-17-0044.1>
- Rignot, E., Jacobs, S., Mouginot, J., & Scheuchl, B. (2013). Ice-shelf melting around Antarctica. *Science*, 341(6143), 266–270. <https://doi.org/10.1126/science.1235798>
- Rintoul, S. R. (2018). The global influence of localized dynamics in the Southern Ocean. *Nature*, 558(7709), 209–218. <https://doi.org/10.1038/s41586-018-0182-3>
- Roach, C. J., & Speer, K. (2019). Exchange of water between the Ross gyre and ACC assessed by lagrangian particle tracking. *Journal of Geophysical Research: Oceans*, 124(7), 4631–4643. <https://doi.org/10.1029/2018jc014845>
- Ruddick, B. (1983). A practical indicator of the stability of the water column to double-diffusive activity. *Deep Sea Research Part A: Oceanographic Research Papers*, 30(10), 1105–1107. [https://doi.org/10.1016/0198-0149\(83\)90063-8](https://doi.org/10.1016/0198-0149(83)90063-8)
- Ruddick, B., & Hebert, D. (1988). The mixing of meddy “Sharon”. Elsevier Oceanography Series (Vol. 46, pp. 249–261). Elsevier. [https://doi.org/10.1016/s0422-9894\(08\)70551-8](https://doi.org/10.1016/s0422-9894(08)70551-8)
- Ruddick, B., & Kerr, O. (2003). Oceanic thermohaline intrusions: Theory. *Progress in Oceanography*, 56(3–4), 483–497. [https://doi.org/10.1016/s0079-6611\(03\)00029-6](https://doi.org/10.1016/s0079-6611(03)00029-6)
- Shakespeare, C. J. (2016). Curved density fronts: Cyclogeostrophic adjustment and frontogenesis. *Journal of Physical Oceanography*, 46(10), 3193–3207. <https://doi.org/10.1175/jpo-d-16-0137.1>
- Shaw, W. J., & Stanton, T. P. (2014). Dynamic and double-diffusive instabilities in a weak pycnocline. part i: Observations of heat flux and diffusivity in the vicinity of maud rise, Weddell Sea. *Journal of Physical Oceanography*, 44(8), 1973–1991. <https://doi.org/10.1175/jpo-d-13-042.1>
- Smyth, W., Moum, J., & Caldwell, D. (2001). The efficiency of mixing in turbulent patches: Inferences from direct simulations and microstructure observations. *Journal of Physical Oceanography*, 31(8), 1969–1992. [https://doi.org/10.1175/1520-0485\(2001\)031<1969:teom-it>2.0.co;2](https://doi.org/10.1175/1520-0485(2001)031<1969:teom-it>2.0.co;2)
- Sweeney, C., Smith, W. O., Hales, B., Bidigare, R. R., Carlson, C. A., Codispoti, L., et al. (2000). Nutrient and carbon removal ratios and fluxes in the Ross Sea, Antarctica. *Deep Sea Research Part II: Topical Studies in Oceanography*, 47(15–16), 3395–3421. [https://doi.org/10.1016/s0967-0645\(00\)00073-4](https://doi.org/10.1016/s0967-0645(00)00073-4)
- Thompson, A. F., Stewart, A. L., Spence, P., & Heywood, K. J. (2018). The Antarctic Slope current in a changing climate. *Reviews of Geophysics*, 56(4), 741–770. <https://doi.org/10.1029/2018rg000624>
- von Appen, W.-J., Pickart, R. S., Brink, K. H., & Haine, T. W. (2014). Water column structure and statistics of Denmark Strait Overflow Water cyclones. *Deep Sea Research Part I: Oceanographic Research Papers*, 84, 110–126. <https://doi.org/10.1016/j.dsr.2013.10.007>
- Walsh, D., & Carmack, E. (2003). The nested structure of Arctic thermohaline intrusions. *Ocean Modelling*, 5(3), 267–289. [https://doi.org/10.1016/s1463-5003\(02\)00056-2](https://doi.org/10.1016/s1463-5003(02)00056-2)
- Whitworth, T. (1983). Monitoring the transport of the Antarctic Circumpolar Current at Drake Passage. *Journal of Physical Oceanography*, 13(11), 2045–2057. [https://doi.org/10.1175/1520-0485\(1983\)013<2045:mttota>2.0.co;2](https://doi.org/10.1175/1520-0485(1983)013<2045:mttota>2.0.co;2)
- Wong, A. P., & Riser, S. C. (2011). Profiling float observations of the upper ocean under sea ice off the Wilkes Land coast of Antarctica. *Journal of Physical Oceanography*, 41(6), 1102–1115. <https://doi.org/10.1175/2011jpo4516.1>